Eurasian Journal of Physics and Functional Materials

2026, 10(1), 56-71

Detection system of DGFRS-2 setup: simulation of heavy recoil spectra and radiation limits

D.A. Ibadullayev[1,2,*], A.N. Polyakov[1], M.V. Shumeiko[1], Yu.S. Tsyganov[1], A.A. Voinov[1], Z.Y. Zhang[3], X. Zhang[3]

[1]Joint Institute for Nuclear Research, 141980 Dubna, Russian Federation

[2]Institute of Nuclear Physics, 050032 Almaty, Kazakhstan

[3]State Key Laboratory of Heavy Ion Science and Technology, Institute of Modern Physics,

Chinese Academy of Sciences, Lanzhou 730000, China

E-mail: Ibadullayev@jinr.ru

DOI: **10.32523/ejpfm.2026100104**

Received: 20.02.2026 - after revision

The detection system of the DGFRS-2 setup was employed in long-term experiments using ion beams of ^{40}Ar , ^{48}Ca , ^{50}Ti , and ^{54}Cr from the DC-280 cyclotron at the Flerov Laboratory of Nuclear Reactions (FLNR JINR). The registered energy spectra of recoiled superheavy nuclei were compared to calculated spectra, and satisfactory agreement was achieved. Additionally, radiation effects observed during prolonged irradiation were investigated. These effects included the growth of leakage current in the DSSD focal detector as well as limitations on the use of silicon detectors and the application of ER spectra modeling in long-term experiments. A representative example illustrating the increase in leakage current of a DSSD detector during the experiment is presented. An attempt to predict the lifetime of the DSSD detector in experiments at the DGFRS-2 setup is proposed, based on simple scaling of radiation damage effects using the non-ionizing energy loss (NIEL) concept.

Keywords: superheavy element; separator; double sided silicon detector; leakage current; energy spectra

Introduction

The most profound insights into nuclear structure are often obtained through the study of nuclei under extreme conditions. Superheavy nuclei (SHN) serve

as a prime example, as their large proton numbers lead to intense Coulomb repulsion, making them inherently unstable against spontaneous fission. However, quantum shell effects provide additional stability, enabling the existence of these nuclei. Several theoretical models predict an "island of stability" [1] — a region around element 114 (flerovium), where nuclei are expected to exhibit significantly increased half-lives relative to those outside this region.

Since 1998, the FLNR at JINR has conducted a systematic program of superheavy element synthesis using the Dubna Gas-Filled Recoil Separator (DGFRS) [2, 3]. These experiments employed complete fusion reactions between ^{48}Ca ion beams and actinide targets. Between 1998 and 2002, new elements from Flerovium (114) to Oganesson (118) were discovered at FLNR in reactions of ^{48}Ca with actinide targets of ^{242,244}Pu, ^{243}Am, ^{245,248}Cm, ^{249}Bk, ^{249}Cf [4–7]. Several of these findings were later independently confirmed at other international facilities, including SHIP, TASCA (GSI, Germany), BGS (Berkeley, USA), GARIS (RIKEN, Japan) and SHANS-1, SHANS-2 (IMP, China) [8–14].

The synthesis of these elements was made possible by the use of advanced gas-filled recoil separators and highly sensitive detection systems capable of identifying rare α-decay chains and spontaneous fission events amidst substantial background. These systems were crucial in reactions of the type $^{48}\mathrm{Ca} +$ actinide target $\rightarrow$ SHN $+ xn$, carried out at the U-400 cyclotron. The observed production cross sections range from 0.1 to 10 pb. However, future experiments on the synthesis of elements with $Z > 118$ involving heavier projectiles such as ^{50}Ti and ^{54}Cr are expected to result in significantly reduced cross sections, thereby imposing more stringent requirements on the performance of both separators and detection systems.

For further experiments, the new Superheavy Element Factory and the DGFRS-2 separator were put into operation in 2020 [15]. The separator uses intense ($2-7$ $p\mu$A) heavy-ion beams from the DC-280 cyclotron [16]. During this period, the following experiments were carried out [17–20].

Initially, the accelerated ions strike the target. As a result of a complete fusion reaction — occurring with a very low probability — a compound nucleus is formed in an excited state. In order to transit to its ground state without losing protons, the nucleus must emit several neutrons and gamma rays. The recoiled nuclei, ejected from the target due to the momentum imparted by the bombarding particles (e.g., ^{48}Ca), enter the DGFRS-2 separator. There, they are first vertically focused in-flight by the Q_1 quadrupole lens to pass through the gap of the D_1 dipole magnet, which separates heavy nuclei from background particles. Afterward, the recoils are additionally focused by Q_2 (horizontally) and Q_3 (vertically), then pass through the D_2 magnet, which removes lighter particles (such as protons and α-particles), before reaching the detector chamber.

The DGFRS-2 separator is filled with hydrogen gas at a pressure of approximately 0.7 Torr. The detector chamber is separated from the separator volume by a 0.8 μm-thick Mylar window and is filled with pentane gas at 1.2 Torr. To detect rare events of superheavy nuclei decay, the detection module shown in Figure 1 [21–23] was used. Regular leakage current measurements were conducted to assess the detector's radiation damage.

The system is based on a DSSD detector for recording the decays of superheavy nuclei and a low-fission gas module for detecting recoiled nuclei and other charged particles moving outward from the cyclotron. Note that DSSD detectors are widely used in science and not only in facilities such as gas-filled separators [12, 24–29].

1. Energy spectra of recoiled superheavy nuclei detected with the silicon radiation detector

In the experiments on the synthesis of superheavy elements (SHE), a specialized registration method known as the "active correlation technique" is employed. It enables registration of α-decays from daughter products in a virtually background-free mode by switching off the cyclotron beam for the decay time after detecting the ER–α correlation link in real time.

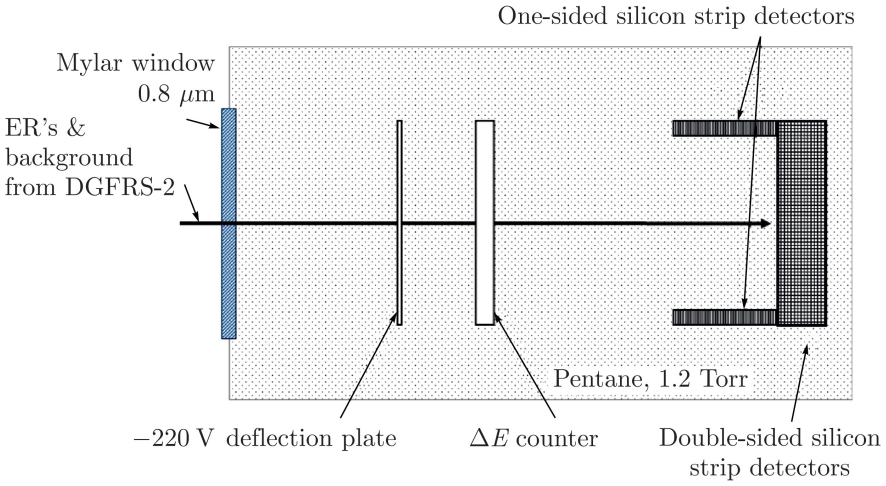

Figure 1. Schematics of the detection module of the DGFRS-2 setup (not to scale).

The idea behind the "active correlations" method for real-time operation is to create two discrete (matrix-based) virtual objects ("detectors") in the memory of the detection system's computer. Specifically, these are the recoil (ER) and alpha particle matrices, each with a discretization of $X \times Y$. Here, X and Y represent the number of horizontal and vertical strips, respectively. Naturally, before this, the experimenter defines the ER and alpha-decay objects as part of the preliminary conditions file.

The matrix elements contain the current time obtained from the hardware (or the Windows system clock). When a signal of α type is received, it is compared with the corresponding element of the ER matrix. If the time difference $t_{ij}(\alpha) - t_{ij}(\mathrm{ER}) < \varepsilon$, the irradiation process is paused for a duration of Δt. If an alpha decay is registered during the beam-off pause, and it falls within a predefined energy range and the same position, the beam-off phase is extended. Edge effects between neighboring strips are naturally taken into account [21, 30]. An alternative version of the trigger is also possible, using ER–α–α instead of the standard ER–α [31]. Over the past two years, a more advanced version of

this method has been tested, replacing the standard algorithm with a flexible algorithm [22, 32, 33]. In essence, the experimenter sets an acceptable level of irradiation time loss, and the system automatically selects the correlation time interval in an adaptive mode. It is believed that this algorithm may be most efficient at titanium beam currents around $10\ p\mu$A or slightly lower. Simplified versions are also possible, such as stopping solely by an alpha-decay signal (if the energy of the studied nuclide is known), or working with correlated signals while ignoring ΔE signals [33]. In detail, this method is described in [21, 30–34]. As a visual example, Figure 2 shows the decay chain of flerovium from the experiment $^{242}\mathrm{Pu} + {}^{48}\mathrm{Ca} \rightarrow {}^{287}\mathrm{Fl} + 3n$.

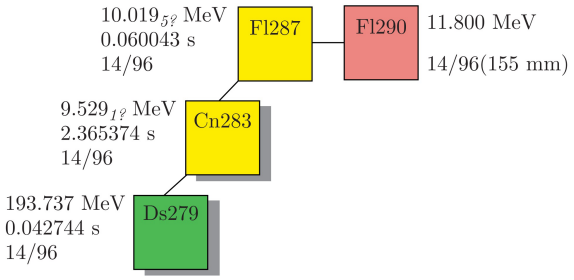

Figure 2. Example of a decay chain of the nucleus ^{287}Fl. Shadows denote beam-off time interval after detecting $ER-\alpha$ sequence in a real time mode. The recoiled nucleus is shown in pink, while the nuclei undergoing alpha decay and spontaneous fission are shown in yellow and green, respectively. The energy, coordinates, and decay time are also indicated.

After the detection system registered an ER–α correlation in real time, the beam was switched off (with a dead time of approximately $100\ \mu$s), and the subsequent decays (indicated by the shaded area) occurred under virtually background-free conditions.

Consequently, understanding the shape of a recoiled heavy nucleus spectrum is relevant for both ongoing experiments and planned efforts to synthesize elements with $Z = 119$ and $Z = 120$ in the foreseeable future, particularly when using heavy-ion beams of ultra-high intensity, up to approximately $\sim 5-10\ p\mu$A.

Figure 3 shows the spectra of the registered energy of nuclei implanted into a silicon detector for the reactions $^{243}\mathrm{Am} + {}^{48}\mathrm{Ca} \rightarrow \mathrm{Mc}^*$ and $^{242}\mathrm{Pu} + {}^{48}\mathrm{Ca} \rightarrow \mathrm{Fl}^*$.

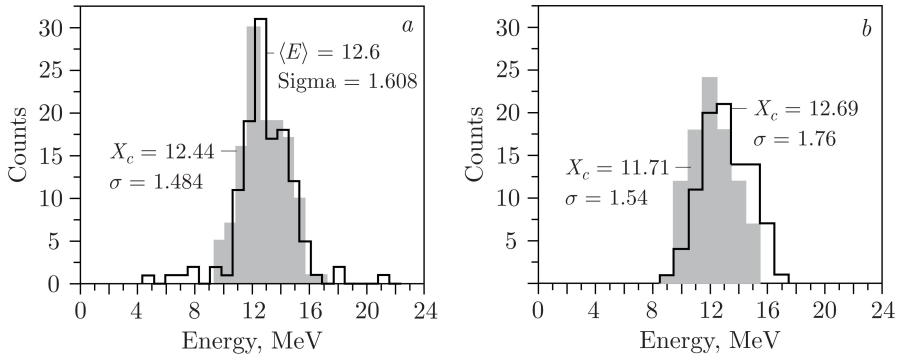

Figure 3. a) Measured (black) and calculated (grey) spectra of Mc ER's. Reaction $^{243}Am + {}^{48}Ca \rightarrow Mc*$. b) Measured (black) and calculated (grey) spectra of Fl ER's. Reaction $^{242}Pu + {}^{48}Ca \rightarrow Fl*$.

On the other hand, it should be noted that there are isolated events outside the $\pm 3\sigma$ standard deviation region. Below, in Figure 4, the recoiled nuclei spectra from the calibration reaction $^{\mathrm{nat}}\mathrm{Yb} + {}^{48}\mathrm{Ca} \rightarrow {}^{217}\mathrm{Th} + 3n$ are shown.

The presence of a right-hand tail in the spectrum is evident, whereas the left side is absent. The nature of these small deviations from the model spectrum may become one of the objectives of our future investigations. However, as a reasonable hypothesis, we can point to two possible processes responsible for the presence of the right-side tail of the distribution:

- channeling effect of heavy ions in silicon [35];
- strong asymmetry of non-ionizing energy loss (NIEL) fluctuations in silicon.

Table 1 below shows the events that fall outside the $\pm 3\sigma$ range of the main distribution. It should be noted that quantitatively these account for no more than approximately 2.8% of the total number of events.

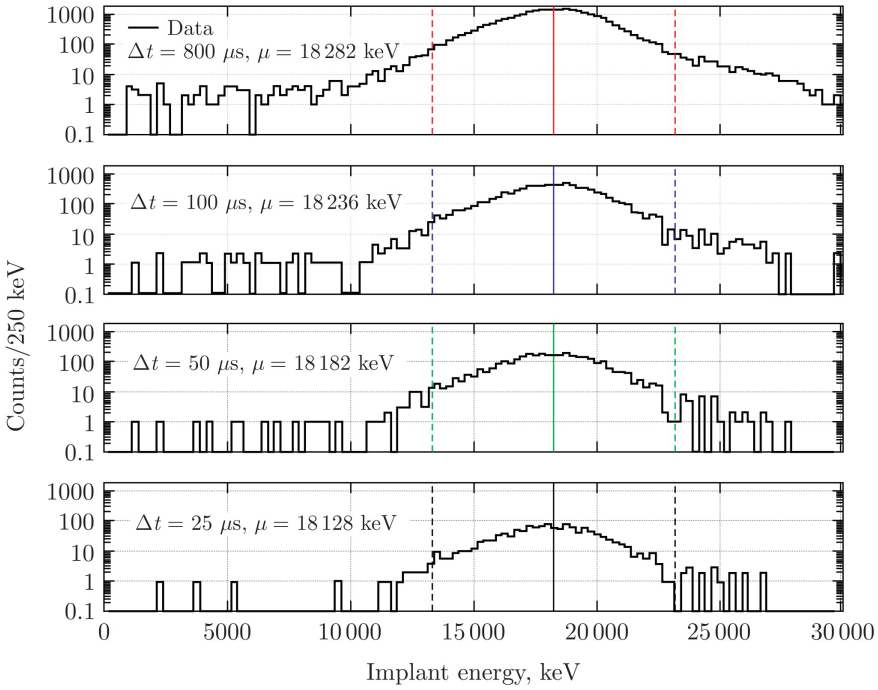

Figure 4. Spectra of ^{217}Th ER for different correlation time intervals (centroids μ and interval values Δt are shown, dashed lines indicate ± 3 sigma interval).

Table 1.
Event distribution outside $\pm 3\sigma$.

^{217}Th $dt(ER-\alpha)$, μs Reaction ^{nat}Yb $+^{48}$Ca	Mean value, keV	Standard deviation	Left / right outside $\pm 3\sigma$, % (with respect to total event number)
25	18128	1656	1.18 / 1.34
50	18182	1677	1.51 / 1.23
100	18236	1639	1.55 / 1.36
800	18282	1625	1.49 / 1.55

On the registered energy spectra of ^{254}No nucleus

When preparing this manuscript, the experiment $^{241}\mathrm{Am} + {}^{48}\mathrm{Ca} \rightarrow \mathrm{Mc}^{*}$ has been successfully finished [13] at the Institute of Modern Physics (Lanzhou, China). During that experiment, a complete fusion nuclear reaction $^{208}\mathrm{Pb} + {}^{48}\mathrm{Ca} \rightarrow {}^{254}\mathrm{No} + 2n$ was used for the sake of calibration and to test the overall electronics readiness. Below, in Figure 5a, spectra of ^{254}No ERs implanted into a DSSD detector for different correlated time intervals are shown. It can be easily seen that for different time intervals the same shapes of these spectra are observed. In Figure 5b, a simulated evaporation-residue (ER) spectrum for nobelium (No) is presented [36]. The difference in the centroid position of about 0.9 MeV is measured and is added to Table 1 for the sake of comparison. Namely, one can accept this result as a local conclusion.

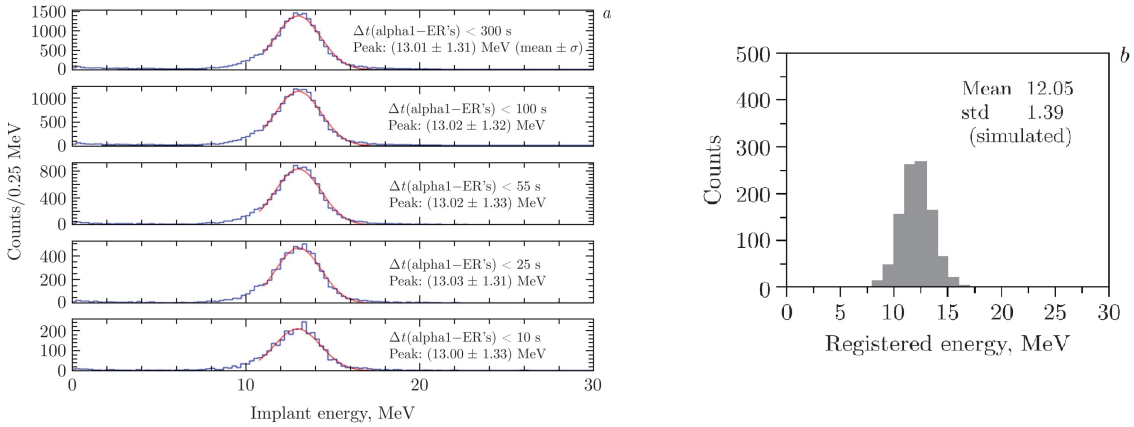

Figure 5. a) The registered energy spectra for ^{254}No nuclei. Correlated times are: 300, 100, 55, 25 and 10 s, respectively (from top to bottom). b) Calculated spectrum of ^{254}No ER's using code from [21].

Reaction $^{249}\mathrm{Bk} + {}^{50}\mathrm{Ti} \rightarrow {}^{296}119 + 3n$

Using the code for generating the spectrum of implanted heavy nuclei [21] and the data from Table 2, the recoiled nucleus spectrum of the isotope $^{296}119$, produced in the fusion–evaporation reaction $^{249}\mathrm{Bk} + {}^{50}\mathrm{Ti} \rightarrow {}^{296}119 + 3n$, was generated. This reaction is considered a promising candidate for the synthesis of element $Z = 119$ at the DGFRS-2 setup in the near future, using an intense titanium ion beam at the DC-280 cyclotron. The resulting spectrum is shown in Fig. 6 along with a Gaussian fit. It is worth noting the high value of the statistical criterion $R^2 = 0.992$.

Additionally, the 99.7% confidence interval is indicated by a dotted line, taking into account Table 2 (seventh row) and [37]. This value, along with its confidence intervals, can be useful for experimenters during the planned experiment at the DGFRS-2 setup in 2026–2027, as only a few decay events of the $^{296}119$ nucleus are expected to be registered due to its very low production cross section [38–41]. This is especially relevant when applying the active correlations method, which is used to significantly suppress background products associated with the operation of the DC-280 cyclotron. Moreover, it is reasonable to adopt this interval as the first approximation for the search for ER–α correlated sequences in real

time (the active correlations method). The second and subsequent approximations can be determined using a “flexible” algorithm that takes into account the “lost” time criterion [31–34,42]. That is, the predicted total irradiation pause time for the target should not exceed a few percent, where this value is set in advance by the experimenter. In the mentioned works (tests), we selected the maximum number of irradiation stops as $N_{\max} = 4$ with a pause duration of 100 s. Thus, the maximum loss did not exceed 0.5% in those tests. It is important to note that the left boundary plays a crucial role, since the distribution of background signals shows a sharp decline toward higher registered energies. Naturally, the second iterative parameter when applying the flexible algorithm in the active correlations method will be the value of the ER–α correlation interval. In addition, it should be kept in mind that expanding this calculation model for the spectrum of the $Z = 119$ nucleus in the reaction $^{249}\mathrm{Bk} + {}^{50}\mathrm{Ti} \rightarrow {}^{296}119 + 3n$, when approaching an irradiation dose by low-energy target-like products $D \rightarrow 10^8$ ions/cm^2, can be achieved by using the actual value of the surface recombination rate (see Sec. 3).

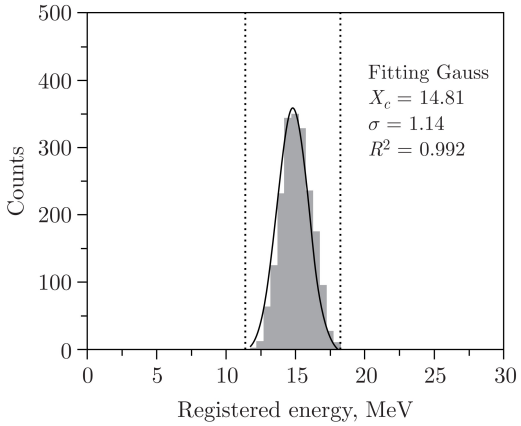

Figure 6. Registered energy spectrum of implanted recoiled nuclei of the isotope $^{296}119$ is shown, with the 99.7% confidence level interval indicated by dotted lines (reaction $^{249}Bk + {}^{50}Ti \rightarrow {}^{296}119 + 3n$).

Radiation effects

The primary manifestation of radiation damage to the detector during long-term experiments is the increase in leakage current. This parameter is commonly used to characterize the operational quality of the detector. For instance, these effects have been studied in [43, 44]. Notably, radiation damage ultimately limits the operational lifetime of silicon detectors in experiments involving ultraintense heavy-ion beams.

Figure 7 illustrates the performance of DSSD detectors Nos. 1–4 in experiments conducted using the DGFRS-2 setup over the past four years. The abscissa represents measurement dates, while the typical "live” beam time ($\sim 2-3$ $p\mu$A) spanned 2–4 months per year. Target-like particles with energies between 0.5–5 MeV (comprising $\sim$ 95–98% of the detector load) were the primary contributors to the detector’s workload. Figure 7b displays the relationship between leakage current and dose for detector No. 2. The estimated dose accuracy

was within $\sim 20\%$. In Figures 7a–d, an increase in detector leakage current can be observed as the experiment progresses. It increases by approximately $1\ \mu$A per day at a temperature of $\sim 27\ ^\circ$C. The dependence of leakage current on dose can be seen in Figure 8.

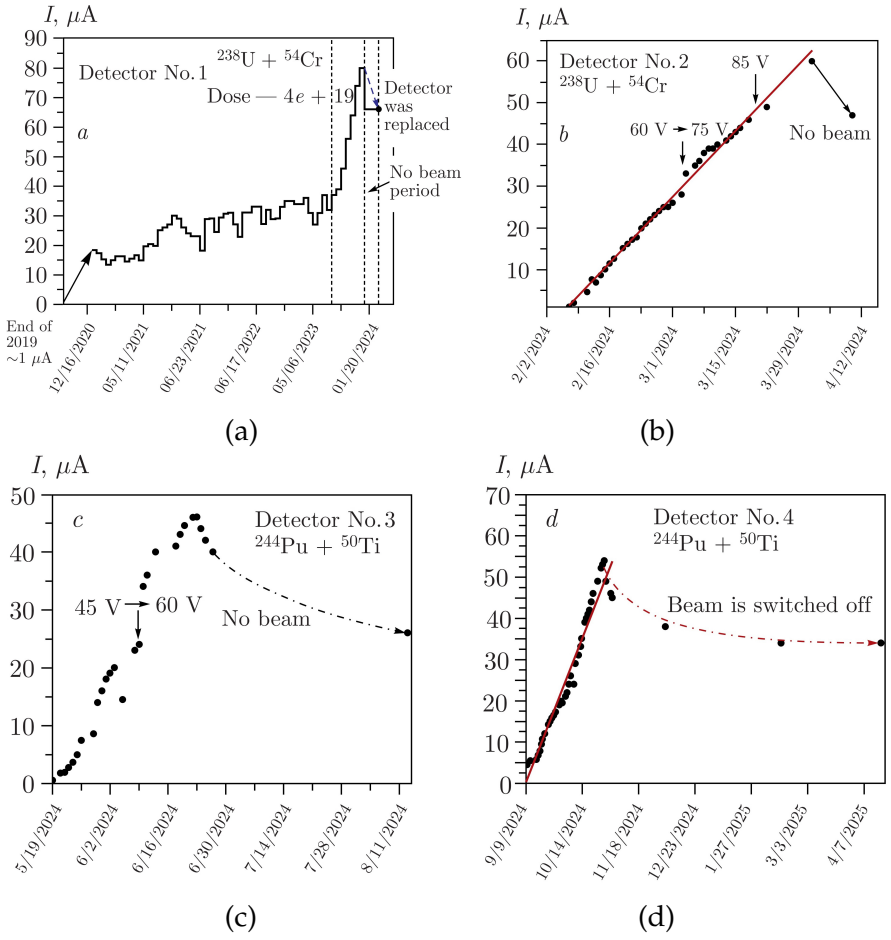

Figure 7. a) Changes in leakage currents against date for detector *No.* 1; b) For detector *No.* 2; c) Changes in leakage currents against date for detector *No.* 3; d) For detector *No.* 4.

Of course, one can easily see that the degradation process of the DSSD detector is quite different for experiments with ^{48}Ca compared to those with ^{50}Ti and ^{54}Cr projectiles. (Dose $\sim 7 \cdot 10^7$ corresponds to the limit for the peak stability region.)

From the perspective of the practical application of silicon detectors in experiments with ultraintense heavy-ion beams – specifically for predicting the detector's in situ lifetime – the dependences (systematics) presented in Fig. 8 are of key importance. This figure illustrates the rate at which the dose approaches the "critical" value, as discussed in [44, 45].

Results and Discussion

All measured amplitudes of recoiled nuclei were obtained strictly in the range of up to an effective dose of $\sim 7 \cdot 10^7$ ions/cm^2. Note that a small percentage

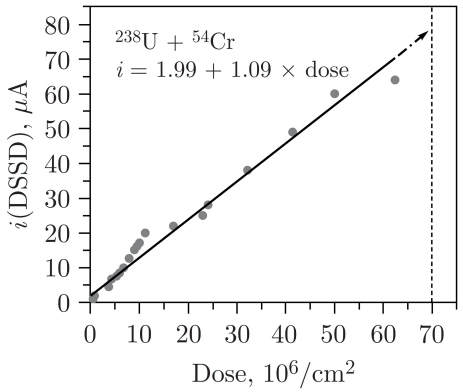

Figure 8. Dependence of leakage current on effective dose value.

of events lies outside the energy interval registered by the DSSD detector and calculated using the code reported in [21]. Table 2 presents typical deviations of the average value of the distribution amplitudes from the value calculated for the reactions listed in the table. The weighted average of the adjustment was:

$$\Delta E = \frac{\Sigma N_i \cdot \Delta_i}{\Sigma N_i} = 0.67, \tag{1}$$

which will be used in subsequent experiments, namely, in the form of a correction formula:

$$\Delta_{CORR} = 0.28 \cdot E_{in} - 0.006 \cdot E_{in}^2 - 0.3, \tag{2}$$

here E_{in} is the energy of the recoiled nucleus at the input of the DSSD detector in MeV, and the average value of the deviation is calculated by the formula:

$$D = \frac{\Sigma d_i \cdot h_i}{\Sigma h_i}, \tag{3}$$

whereas the statistical weight of the deviation is taken as [37, 46]

$$h_i = \frac{\sqrt{N}}{\sigma_i}, \tag{4}$$

It should be noted that the issue of radiation damage scenarios in silicon detectors under exposure to light particles — hadrons — has been studied for the past 20 years within the RD50 collaboration at CERN [47, 48]. The impact of heavier particles, such as ions of various elements, became relevant only a few years ago in connection with the design of the international accelerator complex FAIR (GSI, Darmstadt, Germany) [49, 50]. It is important to emphasize that in our case we deal with extremely hard radiation (e.g., ^{238}U at ~ 6 MeV has a penetration depth of about one micron, meaning that defect formation occurs in the near-surface region). Even if a single implanted uranium atom creates just one level in the silicon bandgap, then at a dose of about $7 \cdot 10^7$ cm^{-2}, the concentration of levels will be $7 \cdot 10^{11}$ cm^{-3}. For comparison, the donor concentration in n-type silicon with a resistivity of approximately 8 k$\Omega \cdot$ cm is equal to $\sim 2.8 \cdot 10^{11}$ cm^{-3}. The dynamics of the transformation of the n-type semiconductor are described in [51]. Typically, the degradation scenario includes

information on how detector characteristics change with increasing radiation dose — such as generation current, electric field, and several others. The role of near-surface defects under the impact of heavy ions is discussed in [52].

It was Kurokawa [43] who first recognized the importance of the non-ionizing energy loss value (Δ_{st}) along the ion path in silicon as a critical parameter. In [44], critical dose values are presented for three groups of ionizing particles: protons, α-particles, and fission fragments. In Figure 9, a second-order polynomial extrapolation is shown to predict the critical dose for 6 MeV ^{238}U ions using both the Wilkins [53] formula and the Ogihara [54] formula. The formula is as follows:

$$\Delta_{st} = 2.33 \cdot 10^{-4} \cdot A^{0.7} \cdot Z^{1.2} \cdot E^{0.5}, \tag{5}$$

where A - mass number, E - energy in Mev, Z - atomic number.

Table 2.
Parameters of recoiled superheavy nuclei (DSSD types BB-17 and BB-24; see `https://www.micronsemiconductor.co.uk`). For all cases, the summary leakage current is lower than 45 μA.

Reaction	$E_{\text{calc}}/\text{std}_{\text{calc}}$	$d = E_{\text{REG}} - E_{\text{CALC}}$	n(event)	Asymmetry $M_{\text{target}}/M_{\text{ion}}$	$d = \langle d_i \rangle$	$\sigma_{\text{center}} = \frac{\sigma}{\sqrt{n}}$ according to CLT
$^{238}\text{U} + ^{40}\text{Ar} \rightarrow \text{Ds}^*$	6.7 / 1.5	−0.4	2	5.95	$\langle 0.78 \rangle$	1.06
$^{242}\text{Pu} + ^{48}\text{Ca} \rightarrow \text{Fl}^*$	11.8 / 1.6	+1.1	99	5.04		0.161
$^{243}\text{Am} + ^{48}\text{Ca} \rightarrow \text{Mc}^*$	12.4 / 1.5	+0.2	125	5.06		0.134
$^{242}\text{Pu} + ^{50}\text{Ti} \rightarrow \text{Lv}^*$	13.0 / 1.9	+1.8	5	4.84		0.85
$^{238}\text{U} + ^{54}\text{Cr} \rightarrow \text{Lv}^*$	18.5 / 2.0	+0.2	1	4.41		2.0
$^{232}\text{Th} + ^{48}\text{Ca} \rightarrow \text{Ds}^*$	13.1 / 1.2	+1.7	9	4.83		0.40
$^{238}\text{U} + ^{48}\text{Ca} \rightarrow \text{Cn}^*$	11.2 / 1.7	+0.9	16	4.96		0.425
$^{208}\text{Pb} + ^{48}\text{Ca} \rightarrow \text{No}^*$	12.1 / 1.39	+0.9	–	4.33	Not taken into account for d calculation	
$^{242}\text{Pu} + ^{48}\text{Ca} \rightarrow ^{287}\text{Fl} + 3n$	11.4 / 2.3	−0.4	25	4.84		0.46 $\langle \sigma_{\text{center}} \rangle = 0.69$

Therefore, as a local summary, one can state that the critical dose for 6 MeV uranium ions is less than 10^8 cm^{-2}. The same result can be obtained using the electric field-independent formula for the pulse height defect from [44, 55], which is:

$$W = \frac{\left[\frac{6W}{W+8} + \frac{B}{1+525W^{-1.407}}\right]}{K}, \tag{6}$$

$$W = K \cdot E, \tag{7}$$

$$K = 6.53 \cdot \frac{10^4}{[Z(Z^{2/3} + 5.81)^{1/2} \cdot (A + 28.1)]}, \tag{8}$$

where B = 18 [56].

Our experience shows that for our DSSD back strips the typical change in FWHM ranges from 33 – 35 keV to 55 – 65 keV. While this is not critical, the peak positions are considered to be unstable.

Note, additionally, that one can obtain nearly the same result by using TRIM [57] calculations of the average number of primary vacancies as the X axis for

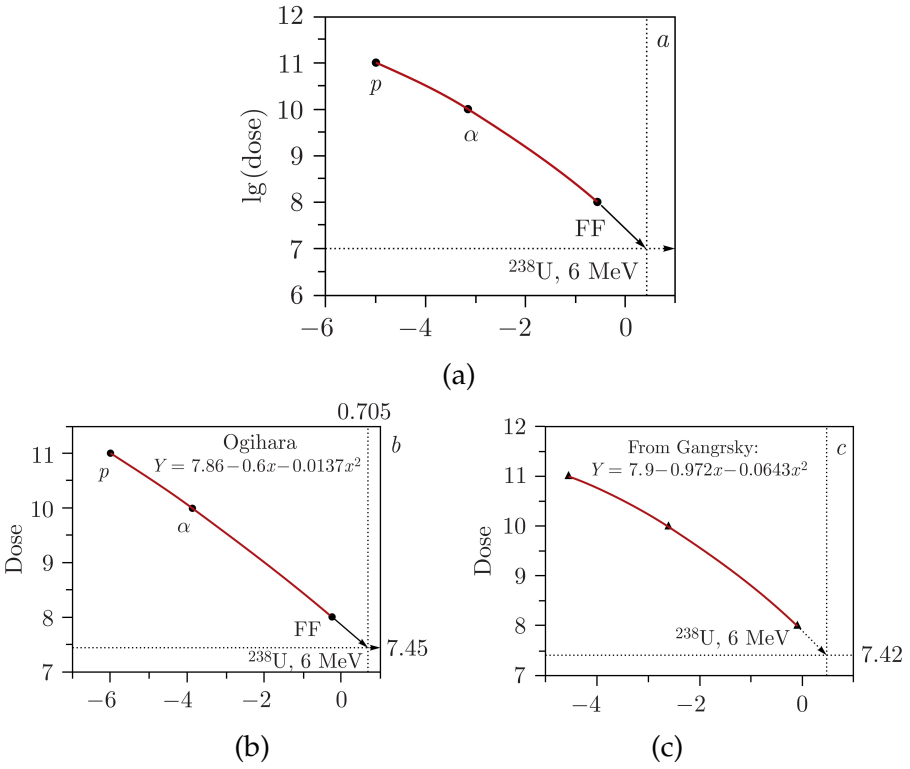

Figure 9. a) Extrapolation of the critical dose value in the region of ^{238}U - 6 MeV based on the Wilkins' formula. The x-axis represents the parameter $lg(\mu)$; b) The same as in Figure 9 a, but based on Ogihara's formula; c) based on formula from work.

interpolation, as shown in Figure 10. A Monte Carlo calculation using event-by-event files from the experiment can be performed (the first 2000 events were taken from the working file PuTi.558 of the $^{242}\text{Pu} + ^{50}\text{Ti} \rightarrow \text{Lv}^*$ reaction). Specifically, each event can be used to calculate both the incoming energy and the individual number of primary vacancies to estimate the effective mean number of vacancies. Of course, each registered energy amplitude should also be corrected individually for the pulse-height effect. For the dependence of the number of vacancies on the registered incoming energy, it is reasonable to apply an analytical approximation.

The use of primary defects, as calculated by TRIM (Figure 10), allows for an extrapolation that is independent of the NIEL (non-ionizing energy loss) method. Naturally, not all primary defects create recombination centers within the silicon forbidden gap. However, as a first-order approximation, it is reasonable to assume that the fraction of defects forming effective recombination levels is proportional to the number of primary defects. Therefore, the number of primary defects can be used as a basis for systematics (the X axis).

The fact that the obtained dose value of approximately $\sim 7 \cdot 10^7$ cm^{-2} coincides with the result derived using the NIEL method makes this approach self-consistent.

As for radiation restrictions on the use of this type of detectors, it is obvious that for more symmetrical ion/target combinations, the number of cases of achieving doses of $\sim 10^8$ ions cm^{-2} this time is significantly shorter. Obviously, when working with heavy-ion beam intensities of ~ 10 $p\mu$A and more, a

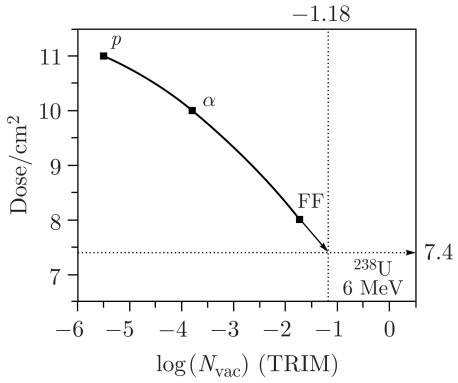

Figure 10. Dose per cm^2 against primary average vacancies number as a parameter (X-axe) for extrapolation procedure.

number of radical changes in the detection system and the DGFRS-2 separator itself will be strictly necessary. These changes are not considered in this article, but we note the unacceptability of trivial approaches, for example, the use of additional absorbers. The reason is a notable decrease in the nuclide implantation depth, which significantly reduces the efficiency of recording the coordinate of a composite signal of α decay (focal DSSD + side detector, see Figure 1).

During the defect formation process, generation–recombination levels are created within the silicon bandgap, which leads to an increased significance of generation–recombination processes, including an increase in leakage current.

Table 3.
Reasonable scenarios to improve the detection system.

Action	Advantage	Disadvantage	An assumed period
1) To set degrader (mylar, aluminum foil)	The simplest	It decreases implantation depth, therefore, to decrease part of energy signal in DSSD when detecting escaping decay	In stage of discussion
2) To change pentane pressure up to 1.5–2.2 Torr	The simple and in contrast to (1) is more flexible	The same as (1)	Late 2025 or early 2026
3) To optimize collimators behind rotating target and some other magnet optics	No need beam time (to a first approximation). See e.g. [61].	Beam time test is strongly required after finishing development process	Early 2026
4) To increase a little bit (up to 0.8–1 Torr) H_2 pressure in the DGFRS-2	Highly likely the same as (2). Can be considered as complementary to (2)	—	Late 2025 or early 2026
5) "Soft" annealing, 50–80 °C	Typical procedure	No warranty of non-destruction of contacts	No plans

For the reverse current arising due to generation–recombination processes in the depletion region, one can write:

$$J_{\text{g-r}} = \frac{en_i d}{\tau_{\text{eff}}}, \tag{9}$$

where e is the elementary charge, d is the width of the depletion layer, n_i is the intrinsic carrier concentration, and τ_{eff} is the effective lifetime of electron–hole pairs [58-60].

It is evident that after the beam is turned off not only the number of recombination levels increases — leading to a decrease in the effective carrier lifetime and, consequently, an increase in leakage current — but also some of the newly formed levels within the silicon bandgap undergo relaxation, as observed in the figures above.

It is important to note, however, that this standard approach does not explain the observed saturation in the decrease of leakage current after the end of the experiment. As a preliminary conclusion of this section, the following points should be mentioned:

- the system has demonstrated good performance and will continue to be used in its current form for asymmetric reactions (e.g., ^{48}Ca , see Figure 5a) in long-term SHE synthesis experiments;
- for reactions involving ^{50}Ti and ^{54}Cr ions, reasonable but not radical adaptation scenarios are possible, as outlined in Table 3;
- as long as the mitigation strategies described in Table 3 remain effective, we do not foresee any radical changes in the near future (up to ~ 2026).

And, of course, in any case, a compromise should be reached between the chosen action ($1-5$) and achieving the maximum possible implantation depth.

Conclusion

In long-term experiments conducted using the DGFRS-2 setup, spectra of recoiled superheavy nuclei with $Z = 114-116$ were measured in [17–20] and found to be in good agreement with computer simulations, with discrepancies limited to a small empirical correction of approximately $6\,\%$. Regarding the negative radiation-induced changes in the leakage current of DSSD detectors, at heavy-ion intensities on the order of $2-3$ $p\mu$A (using ^{54}Cr and ^{50}Ti projectiles), the leakage current can increase by approximately 1 μA per day at a temperature of ~ 27 °C. An attempt was made to roughly estimate the radiation dose limit for DSSD detector applications during irradiation with low-energy target-like products. The detection system can be improved without radical changes for long-term experiments with Ti and Cr ions at intensities above $2-3$ $p\mu$A.

Furthermore, we will continue to enhance the method for calculating spectra of implanted recoiled nuclei in silicon detectors, including the use of more asymmetric distributions for fluctuations in non-ionizing energy loss and taking into account other phenomena that lead to approximately $2.8\,\%$ of events deviating from the main dependence.

Acknowledgement

This work was supported by the Russian Science Foundation and the National Natural Science Foundation of China (Grant No. 25-42-00003).

We thank Dr. A. Sokhatsky for assistance with radiation defects, Dr. V. Salamatin for assistance in upgrading the code simulating the spectrum of heavy nuclei.

References

[1] Yu.Ts. Oganessian, K.P. Rykaczewski, Phys. Today **68**(8) (2015) 32–38. [*CrossRef*]
[2] Yu.Ts. Oganessian, V.K. Utyonkov, Rep. Prog. Phys. **78** (2015) 036301. [*CrossRef*]
[3] Yu.Ts. Oganessian, V.K. Utyonkov, Nucl. Phys. A **944** (2015) 62–98. [*CrossRef*]
[4] Yu.Ts. Oganessian et al., Physical Review C **74**(4) (2006) 044602. [*CrossRef*]
[5] Yu.Ts. Oganessian et al., Physical Review C **69** (2004) 021601. [*CrossRef*]
[6] Yu.Ts. Oganessian et al., Physical Review C **72** (2005) 034611. [*CrossRef*]
[7] Yu.Ts. Oganessian et al., Physical Review Letters **104** (2010) 142502. [*CrossRef*]
[8] L. Stavsetra et al., Physical Review Letters **103** (2009) 132502. [*CrossRef*]
[9] J. Khuyagbaatar et al., Physical Review Letters **112** (2014) 172501. [*CrossRef*]
[10] Kosuke Morita et al., Journal of the Physical Society of Japan **73**(10) (2004) 2593–2596. [*CrossRef*]
[11] J.M. Gates et al., Physical Review C **92** (2015) 021301. [*CrossRef*]
[12] D.W. Luo et al., Nucl. Instrum and Meth. in Phys. Res. A **1075** (2025) 170333. [*CrossRef*]
[13] X.Y. Huang et al., Chinese Physics Letters **43**(1) (2026) 010101. [*CrossRef*]
[14] S.Y. Xu et al., Nucl. Instrum and Meth. in Phys. Res. A **1050** (2023) 168113. [*CrossRef*]
[15] Yu.Ts. Oganessian et al., Nucl. Instrum and Meth. in Phys. Res. A **1033** (2022) 166640. [*CrossRef*]
[16] G.G. Gulbekian et al., Proceedings of the 21st International Conference on Cyclotrons and their Applications (2016) 278–280.
[17] Yu.Ts. Oganessian et al., Physical Review C **106** (2022) L031301. [*CrossRef*]
[18] Yu.Ts. Oganessian et al., Physical Review C **106** (2022) 024612. [*CrossRef*]
[19] Yu.Ts. Oganessian et al., Physical Review C **106** (2022) 064306. [*CrossRef*]
[20] Yu.Ts. Oganessian et al., Physical Review C **108** (2023) 024611. [*CrossRef*]
[21] D. Ibadullayev et al., Journal of Instrumentation **18** (2023) P05010. [*CrossRef*]
[22] D. Ibadullayev et al., Eurasian Journal of Physics and Functional Materials **6** (2022) 18–31. [*CrossRef*]
[23] D. Ibadullayev et al., Applied Radiation and Isotopes **212** (2024) 111431. [*CrossRef*]
[24] Shinichiro Takeda et al., Nucl. Instrum and Meth. in Phys. Res. A **579**(2) (2007) 859-865. [*CrossRef*]
[25] C.J. Gross et al., Nucl. Instrum and Meth. in Phys. Res. A **450** (2000) 12–29. [*CrossRef*]
[26] R. Grzywacz et al., Nucl. Instrum. and Meth. in Phys. Res. B **261** (2007) 1103–1106. [*CrossRef*]
[27] E.T. Gregor, Bachelor Thesis (TU, Munich, 2010). [*Web Link*]
[28] A.V. Gorshkov, Doctoral Thesis (2009) 155 p. [*Web Link*]
[29] Yu.S. Tsyganov, D. Ibadullayev, ArXiV 2308.02600 (2023). [*CrossRef*]
[30] Yu.S. Tsyganov et al., ArXiV 2305.13344 (2023). [*CrossRef*]
[31] Yu.S. Tsyganov et al., Phys. of Elem. Part. and Atomic Nuclei **49**(6) (2018) 1036–1045. [*CrossRef*]

[32] Yu.S. Tsyganov et al., Acta Physica Polonica B Proceedings Supplement **14**(4) (2021) 767–774. [*CrossRef*]
[33] Yu.S. Tsyganov et al., Physics of Atomic Nuclei **88**(2) (2025) 332–337. [*CrossRef*]
[34] D. Ibadullayev et al., Acta Physica Polonica B Proceedings Supplement **14** (2021) 873-878. [*CrossRef*]
[35] A.A. Alexandrov, PHD Thesis, Moscow Enginering and Phys. Institute, Moscow (1989) 20 p. (In Russian) [*Web Link*].
[36] S.Y. Xu et al., Physical Review C **112**(3) (2025) 034315. [*CrossRef*]
[37] D.J. Hudson, CLT, Geneva, (Russian Edition, Moscow 1967) (1964) 54-56. [*Web Link*].
[38] Yu.Ts. Oganessian et al., Physival Review C **112** (2025) 014603. [*CrossRef*]
[39] Yu.Ts. Oganessian et al., Physival Review C **113** (2026) 014614. [*CrossRef*]
[40] D. Ibadullayev, Report on Topical Workshop on SuperHeavy Element Synthesis (Beijing Normal University, Beijing, China, 2024). [*Web Link*]
[41] N. Kovrizhnykh, Report on TASCA Workshop (GSI, Darmstadt, Germany, 2025). [*Web Link*]
[42] D. Ibadullayev et al., Phys.of Atomic Nuclei **85**(12) (2022) 1981–1987. [*CrossRef*]
[43] M. Kurokawa et al., IEEE Transaction on nuclear science **42**(3) (1995). [*CrossRef*]
[44] Yu.P. Gangrsky et al., Registration and spectrometry of fission fragments (Moscow: Energoizdat, 1992) 312 p. (In Russian). [*Web Link*]
[45] V.F. Kushniruk, JINR Communications P13-11933 (1978) 22 p. [*Web Link*]
[46] D. Hudson, Statistics for Physicists (MIR, 1972) 296 p. (In Russian). [*Google Scholar*]
[47] V.A. Van Lint, Nucl. Instrum. and Meth. A **253** (1987) 453–459. [*CrossRef*]
[48] G. Lindstrom et. al., Nucl. Instrum. Meth. A **466**(2) (2001) 308–326. [*CrossRef*] 0
[49] FAIR – Facility for Antiproton and Ion Research in Europe. [*Web Link*]
[50] V. Eremin et al., Journal of Instrumentation **12** (2017) C03001. [*CrossRef*]
[51] M. Moll, PhD Thesis (Hamburg, 1999) 251 p. [*Web Link*]
[52] V.N. Bugrov et al., Izv. Akad. Nauk SSSR, Ser. Fiz. **50**(5) (1986) 1009-1015. [*Web Link*]
[53] B.D. Wilkins et al., Nucl. Instrum. Meth. **92** (1971) 381. [*CrossRef*]
[54] M. Ogihara et al., Nuclear Instruments and Methods in Physics Research A **251**(2) (1986) 313–320. [*CrossRef*]
[55] S.B. Kaufman et al., Nuclear Instruments and Methods in Physics Research **115** (1974) 47–55. [*CrossRef*]
[56] R.P. Shmitt et al., Nucl.Phys. A **279** (1977) 141–158. [*CrossRef*]
[57] J.F. Ziegler, Code SRIM-2013. [*Web Link*]
[58] N.M. Gnuchev, Electronic Devices: Physical Foundations of Electronics. Ed. by Politechnical University (Saint Petersburg, 2013) 1–94. (In Russian) [*Web Link*]
[59] G.E. Pikus, Fundamentals of Semiconductor Detector Theory (Moscow: Nauka, 1965) p. 450. (In Russian) [*Web Link*]

[60] P. Lynch, A. Nicolaides, Worked Examples in Physical Electronics (London : Harrap, 1972) p. 237 [*Web Link*]
[61] D.I. Solovyev et al., Journal of Instrumentation **17** (2022) P07033. [*CrossRef*]